

# Constraints on the Intergalactic Magnetic Field from Bow Ties in the Gamma-ray Sky

Paul Tiede,<sup>1</sup> Avery E. Broderick,<sup>1,2</sup> Mohamad Shalaby,<sup>1,2,3</sup> Christoph Pfrommer,<sup>4</sup> Ewald Puchwein,<sup>5</sup> Philip Chang,<sup>6</sup> and Astrid Lamberts<sup>7</sup>

<sup>1</sup>*Department of Physics and Astronomy, University of Waterloo,  
200 University Avenue West, Waterloo, ON, N2L 3G1, Canada*

<sup>2</sup>*Perimeter Institute for Theoretical Physics, 31 Caroline Street North, Waterloo, ON, N2L 2Y5, Canada*

<sup>3</sup>*Department of Physics, Faculty of Science, Cairo University, Giza 12613, Egypt*

<sup>4</sup>*Heidelberg Institute for Theoretical Studies, Schloss-Wolfsbrunnengasse 35, D-69118 Heidelberg, Germany*

<sup>5</sup>*Institute of Astronomy and Kavli Institute for Cosmology,  
University of Cambridge, Madingley Road, Cambridge, CB3 0HA, UK*

<sup>6</sup>*Department of Physics, University of Wisconsin-Milwaukee,  
3135 N. Maryland Ave., Milwaukee, WI 53211, USA*

<sup>7</sup>*Theoretical Astrophysics, California Institute of Technology, Pasadena, CA 91125, USA*

(Dated: February 10, 2017)

Pair creation on the cosmic infrared background and subsequent inverse-Compton scattering on the CMB potentially reprocesses the TeV emission of blazars into faint GeV halos with structures sensitive to intergalactic magnetic fields (IGMF). We attempt to detect such halos exploiting their highly anisotropic shape. Their persistent nondetection excludes at greater than  $3.9\sigma$  an IGMF with correlation lengths  $>100$  Mpc and current-day strengths in the range  $10^{-16}$  to  $10^{-15}$  G, and at  $2\sigma$  from  $10^{-17}$  to  $10^{-14}$  G, covering the range implied by gamma-ray spectra of nearby TeV emitters. Alternatively, plasma processes could pre-empt the inverse-Compton cascade.

PACS numbers: 95.85.Pw — 98.62.En — 98.54.Cm

*Introduction.*— Astronomical magnetic fields appear on scales ranging from the terrestrial to those of galaxy clusters, the latter spanning many Mpc. Within all of these systems magnetic fields are believed to play a variety of important roles. These include providing additional pressure components [1], mediating the magneto-hydrodynamic turbulence [2], providing and limiting the effective viscosity that transports angular momentum in accretion disks [3] and mediates collapse [4, 5], contributing to the acceleration of high energy particles, e.g., cosmic rays [6], and dictating their subsequent propagation [7, 8] as well as diffusion of thermal energy and momentum in weakly collisional and collisionless systems [9].

Observed astrophysical magnetic fields are likely amplified from weak primordial seed fields. These seed fields may originate from Biermann battery processes [10], electroweak or quantum chromo-dynamics phase transitions in the early universe, or during cosmic inflation. Biermann battery processes can naturally generate magnetic fields when temperature and density gradients are not parallel, resulting in electric fields that have a curl and providing a source for the magnetic field. Typically, these processes have a correlation length that reflects the length scales associated with the temperature and density gradients [10, 11], and generate small scale ( $\sim 10$  kpc) fields ( $B \sim 10^{-20}$  G), which can be amplified by the action of a dynamo to  $\mu$ G fields observed in galaxies today [1, 12, 13].

By their nature, fields generated in primordial processes may be present in the intergalactic medium as the IGMF. While the general nature of these fields is still unknown, causal constraints limit the coherent length scales

of primordial fields generated from post-inflation mechanism, e.g., phase transitions, to small comoving scales, typically  $< 10$  kpc [11]. Small scale fields may seed large scale fields through the inverse cascade up to  $\sim 0.1$  Mpc, i.e., the sonic scale of  $10^4$  K gas over the age of the universe [14].

To generate large-scale ( $\gtrsim 1$  Mpc) volume-filling fields, seed fields must have been generated prior to or during inflation [15, 16] or from second-order interactions between the photon and electron fluid prior to recombination [17]. In the former case, additional physics of super-adiabatic magnetic amplification [18] is needed to keep these fields relevant today. This leaves the strength of these inflationary fields unconstrained [11]. In the latter case, the expected comoving field strength is  $B \sim 10^{-24}$  G.

Probing these primordial fields is difficult, but some constraints can be set on a large-scale IGMF. The best direct upper limits on the strength of a putative large-scale IGMF to date come from the impact of such fields on the Cosmic Microwave Background (CMB), roughly  $10^{-9}$  G, followed closely by limits arising from Faraday rotation measurements, roughly  $10^{-9}$  to  $10^{-8}$  G depending weakly on the coherence length of the field  $\lambda_B$  [19]. Indirect limits on large-scale IGMFs can be obtained from the rotation measures of galaxy clusters, constraining the IGMF on scales exceeding a Mpc to be less than  $10^{-12}$  G [19, 20]. In contrast, indirect lower-limits can be placed by the observed absence of inverse-Compton gamma-ray cascades.

Very-high energy gamma rays (VHEGRs), with energies exceeding  $E > 100$  GeV, lie above the pair-creation threshold with the infrared background [21, 22]. As a

result, the mean free path of VHEGRs in the nearby universe is  $10^2(1+z)^{-4.5}(E/6\text{ TeV})^{-1}\text{ Mpc}$  [23]. That is, while VHEGRs can traverse intergalactic distances, they are absorbed on cosmological distances, producing highly relativistic beams of electron-positron pairs (i.e., Lorentz factors of order  $10^6$ ). This redshift-dependent absorption of high energy gamma rays has been observed [24] and subsequently used to probe the infrared background [25–27].

In the absence of any other process, e.g., collective beam-plasma instabilities [23], these beams will inverse-Compton cool by upscattering cosmic microwave background (CMB) photons to GeV energies. That is, this chain of events would effectively reprocess the TeV emission of AGN into GeV emission. Thus, bright, nearby, extragalactic TeV sources should exhibit a GeV bump that is correlated with their TeV spectral energy distribution (SED). Stringent limits have been placed by *Fermi* on the existence of such a GeV bump already, effectively excluding such a feature in several TeV sources [19, 28].

Presuming that inverse-Compton cooling dominates the evolution of the beams, these non-detections provide indirect, circumstantial evidence for the existence of a strong IGMF, with  $B > 10^{-15}\text{ G}$  to  $10^{-17}\text{ G}$ , depending on the particular extragalactic background light model employed [19, 29, 30]. This assumes that the duty cycle of the gamma-ray blazars is comparable to that observed for the radio mode in AGN, roughly  $10^6\text{ yr}$ ; shorter duty cycles could result in GeV echos that lag behind the initial VHEGR emission by long times, resulting in a weaker limit:  $B > 10^{-17}\text{ G}$  [29, 31]. Such an IGMF would deflect the resulting pairs, whose inverse-Compton emission would then be highly beamed away from us, naturally removing the GeV bump. However, at the same time, this would open the door to the direct detection of the IGMF through the observation of GeV halos surrounding intrinsically gamma-ray bright objects, for which the inverse-Compton emission is beamed into our line of sight.

A number of searches for inverse-Compton halos using the publicly available *Fermi* observations have been performed, yielding contradictory claims but no convincing evidence for their presence to date [32–35]. All have focused on the large radial extent of the gamma-ray halos, typically subtending many degrees. However, this is generally degenerate with the point spread function (PSF) of *Fermi*’s Large Area Telescope (LAT), which until recently was highly uncertain [33, 36]. As result, even when detections are claimed they remain plagued by large systematic uncertainties.

*Method.*— In two companion publications [37, 38] we have demonstrated that these inverse-Compton halos are expected to be highly anisotropic (see also [39, 40]). This originates from different physical origins for a small-scale, tangled IGMF ( $\lambda_B \ll 3\text{ Mpc}$ ) and a large-scale, uniform IGMF ( $\lambda_B > 100\text{ Mpc}$ ). For the latter, of interest here, this is due to extreme beaming of the inverse-Compton

emission coupled with the geometric conditions upon the gyration of the particles. This typically produces a bilateral, narrowly beamed halo, the two lobes being due to the opposite gyration directions of the electrons and positrons [37].

In [38] we demonstrated that existing *Fermi* observations should permit the detection of a large-scale IGMF with strengths comparable to those implied by the absence of GeV bumps in nearby TeV sources, i.e.,  $10^{-16}$  to  $10^{-15}\text{ G}$ . This makes use of stacked one-dimensional angular power spectra that amplify the impact of anisotropy:

$$\mathcal{P}_m = \frac{1}{N_{\text{src}}} \sum_{\text{src}} \frac{1}{N^2} \left| \sum_j e^{im\theta_j} \right|^2, \quad (1)$$

where  $\theta_j$  is the polar angle of the  $j$ th photon defined relative to the position of the central source and an arbitrary direction, and  $N$  the number of photons for the source. For this we make use of the Pass 8R2\_V6 ULTRACLEANVETO event class and limit ourselves to gamma-ray energies between 1 GeV and 100 GeV to avoid large variations in the instrument response. We further apply an energy-dependent and conversion-location-dependent mask (i.e., Front and Back), equal to the 68% inclusion region of the Pass 8R2\_V6 PSF, thus excising the region most dominated by the direct emission from the source.

The existence of a bilateral, jet-like feature appears primarily as an excess of quadrupolar power; with a sufficient number of photons it would produce a sawtooth-like structure in the power spectrum in which even multipoles exhibit an excess. Based upon the source SEDs and Monte Carlo modeling of the *Fermi* source population we have identified sets of *Fermi* objects that are optimized for the detection of the anisotropic halo feature. These necessarily depend upon the assumed strength of the IGMF, with larger IGMFs producing observable halos in more sources and therefore permitting a larger sample that may be profitably stacked. These optimized source lists may be found in Table 1 of [38], with the number of sources ranging from 4 to 18 for current-day strengths of  $B_0 = 10^{-17}\text{ G}$  to  $10^{-14}\text{ G}$  (note that the source-frame field strength is given by  $B = B_0(1+z)^2$ , though due to the small redshifts of the gamma-ray sources employed the two differ by at most a factor of 2). For each an uncontaminated region about each source has been identified via visual inspection. Note that as a result these fields do typically contain many dim sources identified in the Fermi Large Area Telescope Third Source Catalog (3FGL, [41]).

Critically, the anisotropy signal is unlikely to be confused with a number of anticipated systematic contaminants. In principle, these may arise from unknown physics at the TeV source, the LAT response, or unmodeled structures in the gamma-ray sky. In practice,

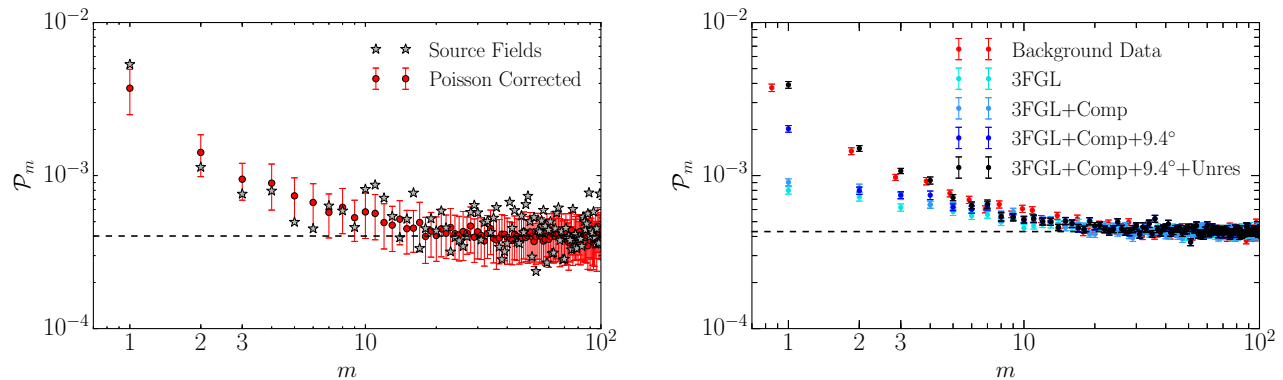


FIG. 1. Left: Comparison of the stacked angular power spectra for the source (optimized for  $10^{-15}$  G) and 507 background fields. The latter have been linearly shifted to adjust for the differing Poisson noise level and the error bars indicate the formal  $1\sigma$  errors for 18 fields assuming that these are Gaussian (for the subsequent simulated backgrounds, this is not found to be the case). Right: Comparison of the observed (red) and reconstructed (black) stacked angular power spectra for the background fields. The formal  $1\sigma$  errors for all 507 background fields are shown. The reconstructed power spectra are constructed using simulated realizations that include the 3FGL, an approximation of its completion, the diffuse structure on scales above  $9.4^\circ$ , and the degree-scale background fluctuations.

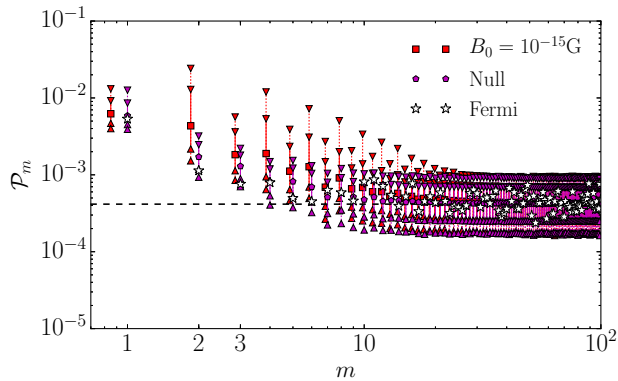


FIG. 2. Comparison of the observed stacked angular power spectrum and that associated with (red) and without (purple) inverse-Compton halos in the presence of a  $10^{-15}$  G IGMF. The triangles show the one-sided  $2\sigma$  and  $3\sigma$  confidence regions inferred from the simulated realizations.

chief among the potential contaminants is the degree-scale substructures in Galactic contribution to the diffuse gamma-ray background. To assess the degree to which these contribute to the stacked angular power spectra we have identified 507 background fields that based on visual inspection we would have identified as empty according to the same criteria used to define the source field regions (see [38]). Stacked, these do indeed show excess power at low multipoles, but do not exhibit a sawtooth-like structure with emphasis on even multipoles (Fig. 1).

*Results.*— We have successfully modeled the background power with a combination of the contaminating 3FGL sources, a random realization of the unresolved completion of the 3FGL source population, the large scale ( $> 9^\circ$ ) gradients, and random realizations of the small-scale gradients. At very high Galactic latitudes ( $|b| > 50^\circ$ ) this last component becomes insignificant, strongly implicating the Galactic contribution as its source. This is shown in the right panel of Fig. 1, subdivided into their origins. More details on the construction of our background power spectrum model and its implementation may be found in the Supplementary Materials.

The stacked angular power spectrum for the optimized source set for  $B_0 = 10^{-15}$  G is shown in the left panel of Fig. 1. As anticipated by the power spectrum from the background fields, there is excess power at low  $m$ . However, this is entirely consistent with that expected for 15 background fields, adjusted via a constant shift for the different Poisson noise level (red points in the left panel of Fig. 1). Thus, there is no evidence for any excess power at low multipoles.

To assess quantitatively the limits upon the IGMF strength that may be placed by the non-detection of excess structure, we employ our background model to generate multiple realizations of optimized *Fermi* source list, with and without inverse-Compton halos present. From these we identify the one-sided confidence level at which a given value of the power may be excluded, i.e., the confidence level (CL), in each direction. Because the stacked powers at different multipoles are strongly correlated, we focus on the quadrupole exclusively when reporting constraints. In principle, we can improve upon

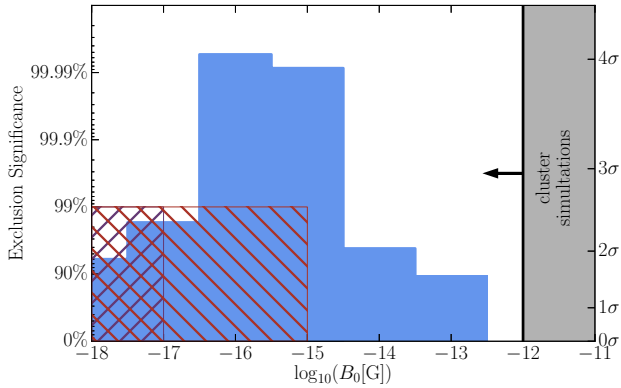


FIG. 3. Significance with which various large-scale IGMF strengths may now be excluded. The blue bars show the limits presented here. The hatched and cross-hatched regions show the range of lower limits implied by [19, 29] depending on assumptions regarding duty cycles and the evolution of the extragalactic background light. Above  $10^{-12}$  G, cluster rotation measures rule out large-scale fields [20].

these by including information at multiple  $m$ ; in practice, this serves to obscure the nature of the test for marginal benefit. Note that because the optimized source lists vary with  $B_0$ , this procedure must be repeated for each IGMF strength.

In Fig. 2 we show the  $2\sigma$  (95.5%) and  $3\sigma$  (99.8%) one-sided confidence levels for each multipole with (red) and without (purple) an inverse-Compton halo. Even without modeling and including the background we can exclude a large-scale IGMF with strength  $B_0 = 10^{-15}$  G by  $2\sigma$ . When the background is included we can exclude our IGMF model at  $3.9\sigma$ . No significant difference is observed when using only Front or Back converted events.

We have repeated this procedure at  $B_0 = 10^{-18}$  G,  $10^{-17}$  G,  $10^{-16}$  G,  $10^{-14}$  G, and  $10^{-13}$  G, generally finding similar results. (For  $B_0 = 10^{-18}$  G and  $10^{-13}$  G we used the optimized source list described in [37] for  $B_0 = 10^{-17}$  G and  $10^{-14}$  G, respectively.) These may be excluded at  $1.9\sigma$ ,  $2.4\sigma$ ,  $3.9\sigma$ ,  $4.0\sigma$ ,  $2.0\sigma$ , and  $1.6\sigma$ , respectively. That is, for present-day field strengths between  $10^{-16}$  G and  $10^{-15}$  G a large-scale IGMF can be excluded at more than  $3.9\sigma$ . At greater than  $2\sigma$  present-day field strengths slightly more than  $10^{-18}$  G to  $10^{-14}$  G a large-scale IGMF can be excluded. These regions are shown in Fig. 3 in comparison to the limits in [29]. Beyond those limits the inverse-Compton halos either become sufficiently small that they are confused with the source (small  $B_0$ ) or extended that they lie beyond the regions about the sources considered (large  $B_0$ ). Nevertheless, we note that this covers the range usually discussed in the context of the indirect SED tests.

In contrast, the null case, i.e., no inverse-Compton halo, is perfectly consistent with the observed stacked an-

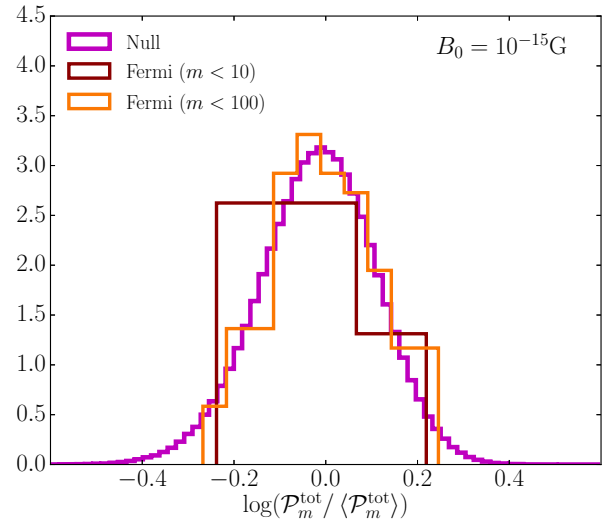


FIG. 4. Probability distribution of the observed power about the mean of the expected power for the  $B_0 = 10^{-15}$  G optimized source sample for  $m < 10$  (brown) and  $m < 100$  (orange). For reference, the distribution observed in the simulated realizations is also shown by the solid purple line. The three are statistically indistinguishable.

gular power. This is evident in Fig. 4, which shows the probability distribution of the simulated and observed power about the simulated median. Not only is each value consistent with being drawn from this distribution, the distributions about the mean is itself similar. Conversely, the ability to reproduce the statistics of the observed stacked angular power provides additional confidence in our ability to adequately model the background model. This remains the case regardless of which optimized source sample is used.

*Conclusions.* — Combined with the SED lower limits, and making modest assumptions regarding the source duty cycles, we can now exclude at more than  $3.9\sigma$  the existence of an IGMF of  $10^{-16} < B_0 < 10^{-15}$  G, and at  $2\sigma$  field strengths of  $10^{-17} < B_0 < 10^{-14}$ , with  $\lambda_B > 100$  Mpc. This provides a strong constraint on models of magnetogenesis that invoke inflationary processes in the early universe, which generate fields on large scales. Nevertheless, this limit may be avoided in one of two ways. First, it is possible that the IGMF morphology is considerably different than that we have presumed. For example, it may be dominated by small-scale structures, for which we expect very little excess power for the source lists that we have considered. Alternatively, its strength may vary substantially on scales only modestly larger than 100 Mpc, resulting in different fields larger than  $10^{-16}$  G to  $10^{-15}$  G in the direction of the sources for which the SED tests were performed and smaller elsewhere. Second, it is possible that the inverse-Compton

halos are preempted by other physical processes. Chief among these are large-scale beam plasma instabilities in the intergalactic medium. The linear growth rates for these far exceed the inverse-Compton cooling times, a conclusion that appears to be robust even when higher order perturbative effects are included [23, 42–44]. However, it does remain to be demonstrated that these instabilities saturate at sufficiently large amplitudes to efficiently extract the energy of the pairs in the nonlinear regime.

A.E.B. and M.S. receive financial support from the Perimeter Institute for Theoretical Physics and the Natural Sciences and Engineering Research Council of Canada through a Discovery Grant. Research at Perimeter Institute is supported by the Government of Canada through Industry Canada and by the Province of Ontario through the Ministry of Research and Innovation. C.P. acknowledges support by the European Research Council under ERC-CoG grant CRAGSMAN-646955 and by the Klaus Tschira Foundation. P.C. gratefully acknowledges support from the NASA ATP program through NASA grant NNX13AH43G, and NSF grant AST-1255469. A.L. receives financial support from an Alfred P. Sloan Research Fellowship, NASA ATP Grant NNX14AH35G, and NSF Collaborative Research Grant 411920 and CAREER grant 1455342. E.P. acknowledges support by the Kavli Foundation.

- 
- [1] R. Beck, *A&A Rev* **24**, 4 (2016).
  - [2] P. Goldreich and S. Sridhar, *Astrophys. J.* **438**, 763 (1995).
  - [3] S. A. Balbus and J. F. Hawley, *Astrophys. J.* **376**, 214 (1991).
  - [4] P. Hennebelle and E. Falgarone, *A&A Rev* **20**, 55 (2012).
  - [5] R. M. Crutcher, *ARA&A* **50**, 29 (2012).
  - [6] R. Blandford and D. Eichler, *Phys. Rep.* **154**, 1 (1987).
  - [7] M. Hanasz and H. Lesch, *Astron. Astrophys.* **412**, 331 (2003).
  - [8] R. Pakmor, C. Pfrommer, C. M. Simpson, and V. Springel, *Astrophys. J. Lett.* **824**, L30 (2016).
  - [9] A. A. Schekochihin, S. C. Cowley, W. Dorland, G. W. Hammett, G. G. Howes, E. Quataert, and T. Tatsuno, *Astrophys. J. Suppl. Ser.* **182**, 310 (2009).
  - [10] R. M. Kulsrud and E. G. Zweibel, *Reports on Progress in Physics* **71**, 046901 (2008).
  - [11] L. M. Widrow, D. Ryu, D. R. G. Schleicher, K. Subramanian, C. G. Tsagas, and R. A. Treumann, *Space Sci. Rev.* **166**, 37 (2012).
  - [12] J. Schober, D. R. G. Schleicher, and R. S. Klessen, *Astron. Astrophys.* **560**, A87 (2013).
  - [13] R. Pakmor, F. A. Gomez, R. J. J. Grand, F. Marinacci, C. M. Simpson, V. Springel, D. J. R. Campbell, C. S. Frenk, T. Guillet, A. Jenkins, C. Pfrommer, and S. D. M. White, submitted (2017), arXiv:1701.07028.
  - [14] D. Ryu, D. R. G. Schleicher, R. A. Treumann, C. G. Tsagas, and L. M. Widrow, *Space Sci. Rev.* **166**, 1 (2012).
  - [15] L. Biermann, *Zeitschrift Naturforschung Teil A* **5**, 65 (1950).
  - [16] M. S. Turner and L. M. Widrow, *Phys. Rev. D* **37**, 2743 (1988).
  - [17] K. Ichiki, K. Takahashi, H. Ohno, H. Hanayama, and N. Sugiyama, *Science* **311**, 827 (2006).
  - [18] C. G. Tsagas and A. Kandus, *Phys. Rev. D* **71**, 123506 (2005).
  - [19] A. Neronov and I. Vovk, *Science* **328**, 73 (2010).
  - [20] K. Dolag, D. Grasso, V. Springel, and I. Tkachev, *JCAP* **1**, 009 (2005).
  - [21] R. J. Gould and G. P. Schröder, *Phys. Rev.* **155**, 1408 (1967).
  - [22] M. H. Salamon and F. W. Stecker, *Astrophys. J.* **493**, 547 (1998).
  - [23] A. E. Broderick, P. Chang, and C. Pfrommer, *Astrophys. J.* **752**, 22 (2012).
  - [24] M. Ackermann *et al.*, *Science* **338**, 1190 (2012).
  - [25] A. Domínguez, J. R. Primack, D. J. Rosario, F. Prada, R. C. Gilmore, S. M. Faber, D. C. Koo, R. S. Somerville, M. A. Pérez-Torres, P. Pérez-González, *et al.*, *Mon. Not. R. Astron. Soc.* **410**, 2556 (2011).
  - [26] R. C. Gilmore, R. S. Somerville, J. R. Primack, and A. Domínguez, *Mon. Not. R. Astron. Soc.* **422**, 3189 (2012).
  - [27] A. Domínguez, J. D. Finke, F. Prada, J. R. Primack, F. S. Kitaura, B. Siana, and D. Paneque, *Astrophys. J.* **770**, 77 (2013).
  - [28] A. Neronov and D. V. Semikoz, *Phys. Rev. D* **80**, 123012 (2009).
  - [29] A. M. Taylor, I. Vovk, and A. Neronov, *Astron. Astrophys.* **529**, A144 (2011).
  - [30] I. Vovk, A. M. Taylor, D. Semikoz, and A. Neronov, *Astrophys. J. Lett.* **747**, L14 (2012).
  - [31] C. D. Dermer, M. Cavadini, S. Razzaque, J. D. Finke, J. Chiang, and B. Lott, *Astrophys. J. Lett.* **733**, L21 (2011).
  - [32] S. Ando and A. Kusenko, *Astrophys. J. Lett.* **722**, L39 (2010).
  - [33] A. Neronov, D. V. Semikoz, P. G. Tinyakov, and I. I. Tkachev, *Astron. Astrophys.* **526**, 90 (2011).
  - [34] M. Ackermann *et al.*, *Astrophys. J.* **765**, 54 (2013).
  - [35] W. Chen, J. H. Buckley, and F. Ferrer, *Phys. Rev. Lett.* **115**, 211103 (2015).
  - [36] M. Ackermann *et al.*, *Astrophys. J. Suppl. Ser.* **203**, 4 (2012).
  - [37] A. E. Broderick, P. Tiede, M. Shalaby, C. Pfrommer, E. Puchwein, P. Chang, and A. Lamberts, *Astrophys. J.* **832**, 109 (2016).
  - [38] P. Tiede, A. E. Broderick, M. Shalaby, C. Pfrommer, E. Puchwein, P. Chang, and A. Lamberts, *Astrophys. J. (submitted)* (2016).
  - [39] A. Neronov, D. Semikoz, M. Kachelriess, S. Ostapchenko, and A. Elyiv, *Astrophys. J. Lett.* **719**, L130 (2010).
  - [40] A. J. Long and T. Vachaspati, *JCAP* **9**, 065 (2015).
  - [41] F. Acero *et al.*, *Astrophys. J. Suppl. Ser.* **218**, 23 (2015).
  - [42] R. Schlickeiser, D. Ibscher, and M. Supsar, *Astrophys. J.* **758**, 102 (2012).
  - [43] P. Chang, A. E. Broderick, C. Pfrommer, E. Puchwein, A. Lamberts, and M. Shalaby, *Astrophys. J.* **797**, 110 (2014).
  - [44] P. Chang, A. E. Broderick, C. Pfrommer, E. Puchwein, A. Lamberts, M. Shalaby, and G. Vasil, *Astrophys. J.* **833**, 118 (2016).

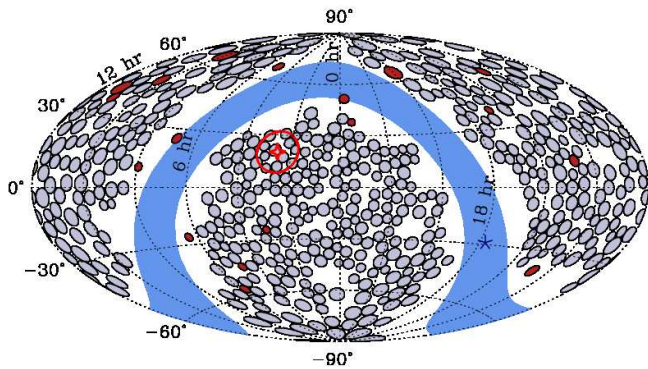


FIG. 5. Aitoff projection of the 18 source (red) and 507 high-latitude background (grey) field locations shown in equatorial coordinates. The region with  $|b| \leq 10^\circ$  is shown in blue and the location of the Galactic Center is shown by the asterisk. For comparison, the location of 1ES 0229+200, the primary source employed by [29], is shown by the orange star; the orange circle indicates the projected 100 Mpc region about 1ES 0229+200. All field locations are circles when viewed directly, the apparent asymmetries are due solely to projection.

### Supplementary Material

*Construction of the Background Model.*— To assess, quantify, and guide the modeling of the background contribution to the stacked angular power spectra we first identified 507 fields with Galactic latitudes more than  $20^\circ$  from the Galactic plane. The locations of these are shown in Fig. 5. Also shown for comparison are the source fields (red). Note that while the background fields appear to nearly cover the sky, the bright point sources in the *Fermi* sky have effectively been excised according to the criteria used in [38] to determine the size of the source fields. That is, all of the bright sources fall into the gaps between the source and background fields. Note that these fields are not devoid of 3FGL sources – sources with fluences less than roughly 40 photons do appear in these background fields and in the source fields. The stacked power spectrum of these 507 fields comprise the background power spectrum that we sought to successfully model.

The model we constructed consists of four components:

1. 3FGL sources
2. Completion of the 3FGL
3. Large-scale gradients ( $> 9^\circ$ )
4. Small-scale gradients ( $\approx 2^\circ$ )

We will discuss the construction of each individually.

The construction of all of these is facilitated by the direct inspection of the *Fermi* sky, obtained from 239557417 s to 487012885 s in mission elapsed time

(MET). A density map of the 1-100 GeV photons in the Front- and Back-converted Pass 8R2\_V6 ULTRACLEANVETO events class, smoothed with a Gaussian kernel. The size of this kernel is informed by typical structure of the point sources, set by the Pass 8R2\_V6 PSF, below which no discernable structure appears. Thus, as our finest resolution map we choose a kernel full-width, half-max (FWHM) of  $1.2^\circ$  is shown in the top row of Fig. 6. The multitude of point sources that comprise the 3FGL are immediately evident. Because the period from which the 3FGL was constructed is roughly half that over which these maps are generated, both exposure differences and source variability will produce significant differences in the anticipated number of photons from each 3FGL object. Therefore, we begin by refitting the individual 3FGL source photon fluences.

We do this by comparing the observed gamma-ray maps smoothed on  $1.2^\circ$  and  $4.7^\circ$  scales to the expected response from the individual point sources. That is, we begin by computing the observed photon density at each of the 3FGL source locations, given by  $n_j^{1.2}$  and  $n_j^{4.7}$ , respectively, for the  $j$ th source. We then simulate the corresponding anticipated fractional response of each individual source at each of the 3FGL positions, i.e., the number density of photons located at the  $j$ th source location associated with  $N_i$  photons from the  $i$ th source are  $f_{ji}^{1.2}N_i$  and  $f_{ji}^{4.7}N_i$  for the two smoothing scales, respectively. In doing this we employ the Pass 8R2\_V6 ULTRACLEANVETO PSFs and assume the spectral index listed in the 3FGL.

In addition to the point sources in the 3FGL there exists a diffuse component associated with gamma-ray emission from Galactic leptons and hadrons. Unlike point sources, this contribution should be similar at both smoothing scales. Thus, we have

$$n_j^s = \bar{n}_j + \sum_i f_{ji}^s N_i \quad (\text{A.2})$$

for some fixed set of diffuse background photon densities,  $\bar{n}_j$ , at both smoothing scales. This may be concurrently solved for the  $\bar{n}_j$  and  $N_i$ , yielding the set of linear equations for the latter,

$$\sum_i (f_{ji}^{1.2} - f_{ji}^{4.7}) N_i = (n_j^{1.2} - n_j^{4.7}). \quad (\text{A.3})$$

We solve this for the  $N_i$ , and subsequently verify that the implied photon density associated with the diffuse background is positive. While this method for estimating the 3FGL source fluences does account for the differing exposures and source variability, it does not account for the possibility of new sources. It is also poorly suited to correcting the fluences of extended sources. We do not anticipate either of these limits to present significant obstacles.

With the individual source fluences we then construct a realization of the 3FGL, smooth it over the appropri-



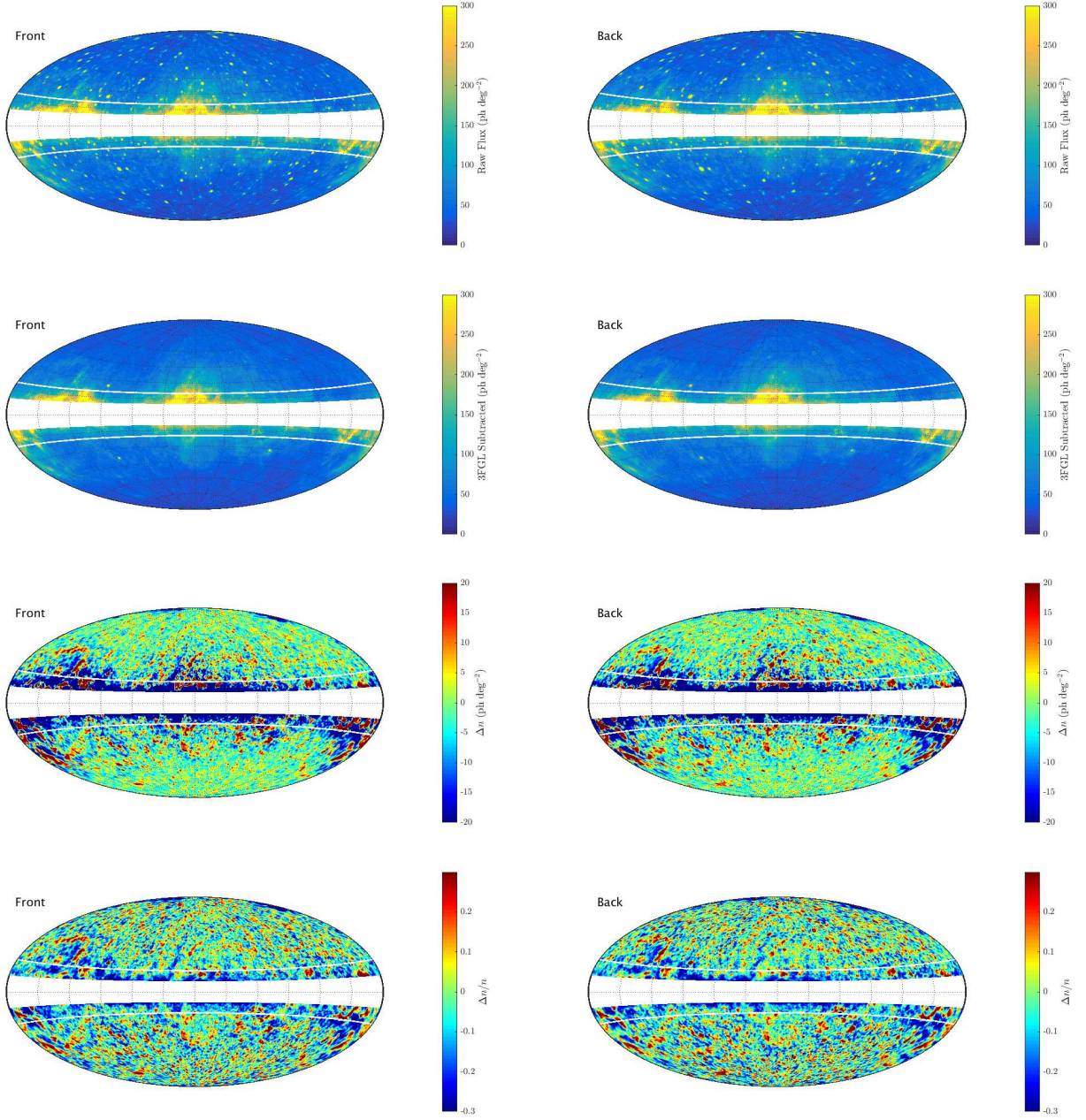


FIG. 6. Aitoff projected maps in Galactic coordinates of the gamma-ray sky at 1-100 GeV for events converted in the front (left) and back (right) detectors. Top: the flux density smoothed with a Gaussian filter with a FWHM of  $1.2^\circ$ . Upper-middle: the flux density smoothed with a Gaussian filter with a FWHM of  $1.2^\circ$  after subtracting the 3FGL sources with their refitted fluences. Lower-middle: the difference of 3FGL subtracted maps smoothed over  $1.2^\circ$  and  $9.4^\circ$ , where the latter is a measure of the large-scale structure in the map, producing an image of the small-scale structure after removal of the 3FGL. Bottom: the fractional difference of the 3FGL subtracted maps smoothed over  $1.2^\circ$  and  $9.4^\circ$ , where the latter is taken as the normalization. In all plots lines of  $|b| = 20^\circ$  are shown in white, and the region for which  $|b| \leq 10^\circ$  has been masked out to remove the Galactic plane.

ate scale, and subtract it from the observed photon density. This is shown for a smooth scale of  $1.2^\circ$  for Front- and Back-converted Pass 8R2\_V6 ULTRACLEANVETO events in the second row of Fig. 6. Apart from a handful

of extended Galactic sources, and up to Poisson fluctuations in the number of sources for the Back-converted map, point sources have been reasonably well removed. In practice, because the background fields specifically ex-

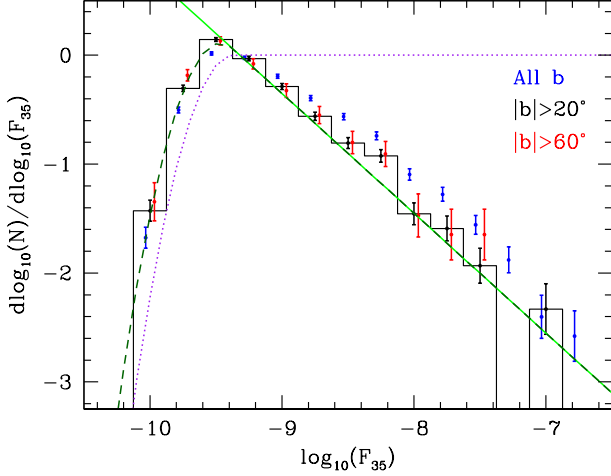


FIG. 7. Flux distribution of 3FGL sources with Galactic latitudes above  $20^\circ$  (black). For comparison the flux distribution of 3FGL sources without any Galactic latitude cut (blue points) and an extreme latitude cut ( $|b| > 60^\circ$ , red points) are also shown; these are offset for clarity. In green we show the single power-law model we assume for the intrinsic flux distribution. The purple dotted line shows the assumed detection efficiency,  $w(F_{35})$ , and the dark-green dashed line shows the associated expected flux distribution.

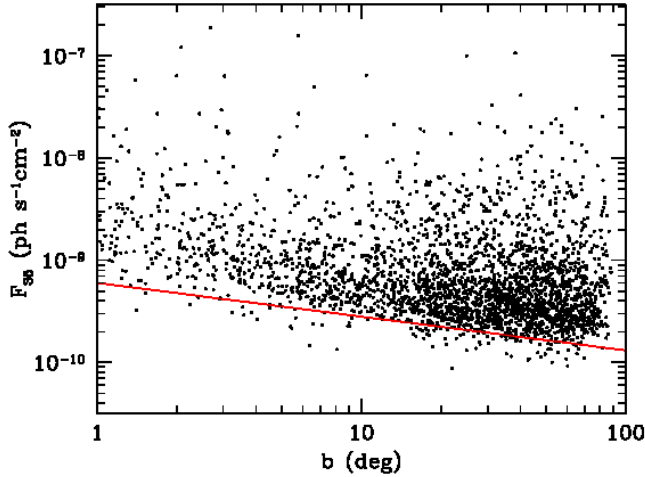


FIG. 8. Flux versus Galactic latitude for the 3FGL catalog. The threshold for detection evolves with latitude as  $b^{-0.33}$ , shown for an appropriate normalization by the red line.

clude bright sources, the details of the 3FGL removal are relatively unimportant. Simply subtracting the 3FGL sources assuming the 3FGL fluxes and fixed exposure produces qualitatively identical results.

The second component, the unresolved completion of the 3FGL, can only be inserted in a statistical sense.

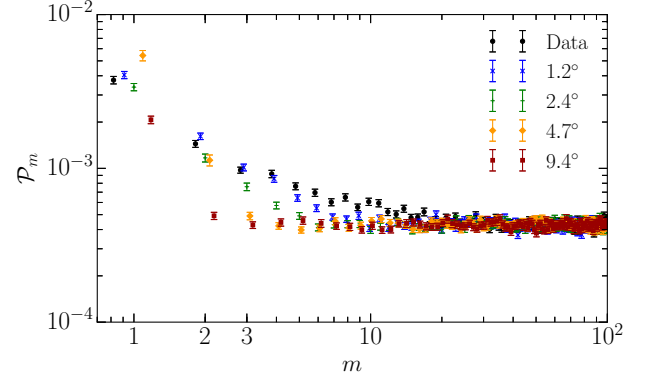


FIG. 9. Stacked angular power spectra of the background fields from the data (black), and for realizations drawn from Gaussian smoothed background maps with various smoothing scales. As the smoothing scale increases power is suppressed at progressively smaller  $m$ . Power at  $m \leq 2$  is associated with structures on roughly a few degree scales.

Ultimately, a complement of sources with the appropriate fluxes are selected and randomly placed within the background/source fields in a manner consistent with the  $9.4^\circ$ -smoothed background. The source fluxes are chosen from the power-law distribution shown in Fig. 7:

$$\frac{d \log_{10}(N)}{d \log_{10} F_{35}} = 0.076 \left( \frac{F_{35}}{10^{-9} \text{ ph s}^{-1} \text{ cm}^{-2}} \right)^{-1.1}. \quad (\text{A.4})$$

This is supplemented with a detection efficiency, which we assume has a log-normal cutoff, i.e.,

$$w(F_{35}) = \begin{cases} \exp[-12.88(\log_{10} F_{35}/F_{\text{th}})^2] & F_{35} < F_{\text{th}} \\ 1 & \text{otherwise.} \end{cases} \quad (\text{A.5})$$

While for the  $|b| > 20^\circ$  population the threshold flux,  $F_{\text{th}}$ , is well described by a single number, in detail it does depend on Galactic latitude. This is clear in Fig. 8, in which there is a trend in the lower envelope of 3FGL fluxes with Galactic latitude, scaling roughly as  $|b|^{-0.33}$ . Therefore, we set

$$F_{\text{th}} = 4.27 \times 10^{-10} |b/90^\circ|^{-0.33} \text{ ph cm}^{-2} \text{ s}^{-1}. \quad (\text{A.6})$$

Note that, despite the fact that the assumed flux distribution produces a formally infinite flux (and is thus unphysical), the condition that photons are observed in integer numbers, i.e., at least one, limits the number of photons observed in practice. That is, for a flux  $F_{35}$  the probability that at least a single photon will be observed is

$$p_1(F_{35}) = 1 - p_0(F_{35}) = 1 - e^{-F_{35}\epsilon} \approx F_{35}\epsilon, \quad (\text{A.7})$$

where  $\epsilon$  is the exposure. Thus, at small fluxes, the probability of observing at least one photon is linearly sup-



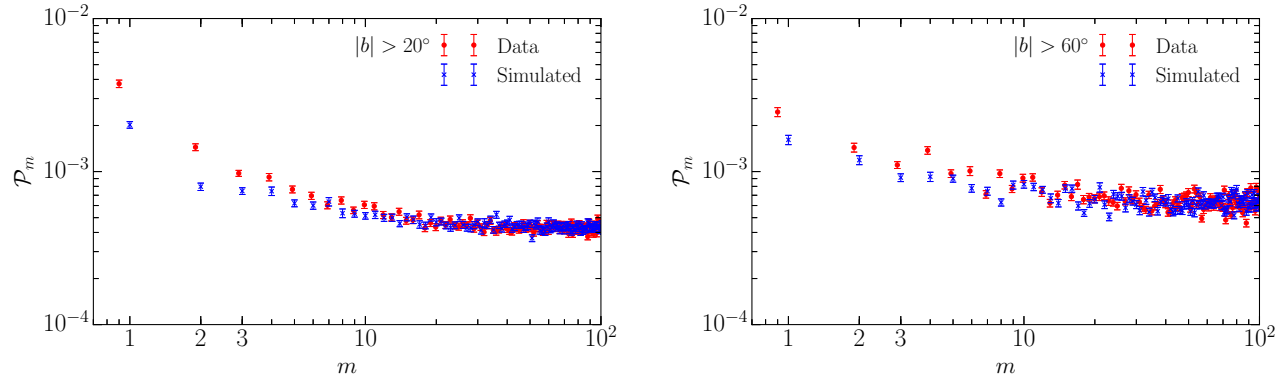


FIG. 10. Stacked angular power spectra for background fields above a given Galactic latitude from the background fields from the data (red), and for simulated realizations that include the 3FGL, an approximation of its completion, and the diffuse structure on scales above  $9.4^\circ$  (blue). The comparison becomes increasingly good as the Galactic latitude increases, strongly suggesting that the disparity is a result of structure in the Galactic foreground.

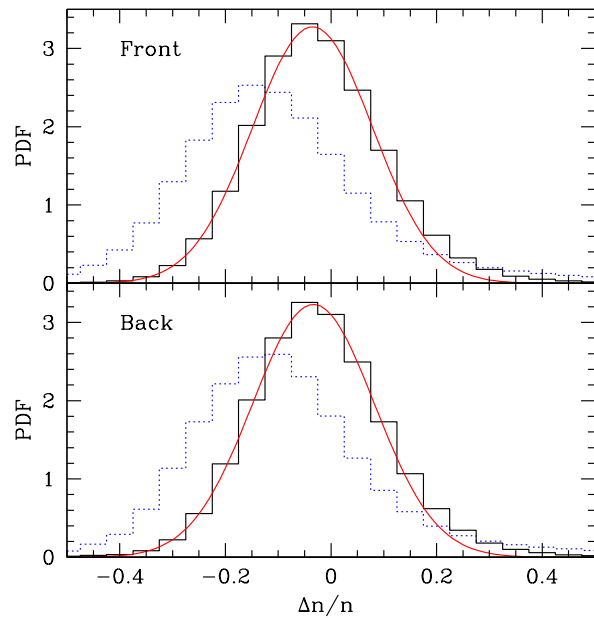


FIG. 11. Fractional flux probability distribution function for fractional fluctuations in the 3FGL subtracted maps of Front-converted (top) and Back-converted (bottom) events, smoothed over  $1.2^\circ$  and  $9.4^\circ$ . A Gaussian fit is shown in red for each, with mean  $-0.035$  and  $-0.033$ , standard deviation  $0.114$  and  $0.115$ , for the Front- and Back-converted event distributions, respectively. In both cases the relative norm of the Gaussian is  $0.94$ . For comparison, in the blue dotted line is the PDF of fractional fluctuations obtained without subtracting the 3FGL sources, giving an indication of the impact of the unresolved completion of the 3FGL. That is, the negative mean and substantial tails at large deviations are likely to be associated with the incomplete source subtraction.

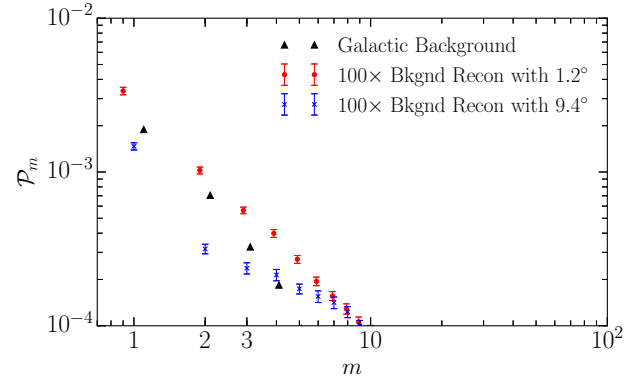


FIG. 12. Comparison of the stacked angular power spectra for simulated background fields using the smoothed, 3FGL-subtracted sky maps smoothed on  $1.2^\circ$  and  $9.4^\circ$  to reconstruct the degree-scale Galactic contribution. To prevent the Poisson noise from dominating the estimate, we randomly draw 100 times more photons from the flux maps than present in the background fields. We model this component as a multipole-dependent log-normal additional component with means and standard deviations chosen to reproduce the difference in power and difference in the variances of the low- and high-resolution angular power spectra.

pressed. Therefore, any flux distribution flatter than  $F_{35}^{-2}$  produces a convergent number of photons.

In practice, the contribution of the unresolved completion of the 3FGL is negligible.

The third component consists of randomly drawing the remaining background photons with a spatial distribution that follows the  $9.4^\circ$ -smoothed map. This modifies the dipole component significantly, though again makes a negligible difference at  $m > 1$ .

Finally, the fourth component consists of an attempt to model the degree-scale fluctuations in the diffuse Galactic background. Stacked angular power spectra generated from realizations of the background fields using smoothed maps of the gamma-ray sky are shown in Fig. 9. Unsurprisingly, larger smoothing scales correspond to less power at large  $m$ . Specifically, at smoothing scales of  $1.2^\circ$  the power above  $m = 5$  is noticeably suppressed. Beyond smoothing scales of  $2.4^\circ$  this suppression extends to  $m \geq 3$ ; by  $9.4^\circ$  only the dipole power remains. This suggests that any missing power at  $m = 2$  is most sensitive to a few degree-scale structures in the diffuse gamma-ray background. Therefore, to clearly identify these we generate difference maps between high ( $1.2^\circ$ ) and low ( $9.4^\circ$ ) smoothing scales. These are shown in the third row of Fig. 6.

Generally, these exhibit a latitude dependent amplitude, falling rapidly with distance from the Galactic plane. This supports their association with Galactic structures. A similar conclusion holds regarding their impact on the stacked angular power spectra. Figure 10 shows a direct comparison between the observed and simulated stacked power spectra, including only the first three components, from the background fields assuming different latitude cuts. When restricted to fields with  $|b| > 60^\circ$  the two are very similar, as anticipated by the large reduction of the Galactic diffuse emission at high latitudes.

In contrast to their absolute amplitudes, the fractional amplitudes in the photon densities is roughly fixed, however (shown in the bottom row of Fig. 6). The PDF of the fractional density fluctuations is well described by the normal distributions, shown in Fig. 11. The mean is offset significantly from zero. This is a natural result from imperfect point source subtraction, likely arising from the failure to subtract unidentified sources. This is supported by the PDF of fractional density fluctuations constructed without any point source subtraction, shown in the dotted blue lines in Fig. 11, which also shows a noted shift to negative fractional flux fluctuations.

The impact of the degree-scale structures in the Galactic diffuse emission is to increase the power at low  $m$ . We quantify this by generating two stacked angular power spectra for the background fields from over-resolved realizations of the gamma-ray sky that include only the initial three components: 3FGL, its completion, and large-scale gradients (Figure 12). These differ in the maps used to generate the last component, the large-scale gradients; one using the map smoothed on  $9.4^\circ$  and the other smoothed on  $1.2^\circ$ . The latter map is statistically indistinguishable from the stacked angular power spectrum obtained from the data directly. The difference between the two is entirely due to the otherwise unresolved degree-scale structures of interest.

We model the angular power due to these small-scale background fluctuations statistically as a multipole-

dependent, log-normal additional component with means and standard deviations chosen to reproduce the difference in power and difference in the variances of the low- and high-resolution angular power spectra. That is, we assume that the power in the high- and low-resolution angular power spectra,  $\mathcal{P}_m^h$  and  $\mathcal{P}_m^l$ , respectively, are related via

$$\mathcal{P}_m^h = \mathcal{P}_m^l + \mathcal{P}_m^{ss} \quad (\text{A.8})$$

where the small-scale structure contribution  $\mathcal{P}_m^{ss}$  is a log-normal random variable, i.e.,  $\mathcal{P}_m^{ss} = \delta_m e^{\sigma_m X}$  for a zero-mean, unit-variance Gaussian random variable  $X$ . The values of  $\delta_m$  and  $\sigma_m$  are fully defined by the means and variances of the  $\mathcal{P}_m^h$  and  $\mathcal{P}_m^l$ ; it is straightforward to show that choosing at each  $m$

$$\delta_m = \sqrt{\frac{\Delta_m^4}{\Delta_m^2 + \Sigma_m^2}}, \quad \sigma_m^2 = \ln \left( \frac{\Sigma_m^2 + \Delta_m^2}{\Delta_m^2} \right), \quad (\text{A.9})$$

where  $\Delta_m$  is the difference in the mean powers and  $\Sigma_m^2$  is the difference in the variances at high and low resolution at a given  $m$ , uniquely reproduces the means and variance of  $\mathcal{P}_m^h$  and  $\mathcal{P}_m^l$ . This is done independently for angular power spectra constructed using Front-converted events, using Back-converted events, and using both Front- and Back-converted events, resulting in slightly different choices for  $\delta_m$  and  $\sigma_m$ . For the last case, the resulting  $\delta_m$  are shown in Figure 12.

*Magnetic Field Strengths.*—In all cases, the precipitous decline in the difference between the high- and low-resolution power spectra results in a rapidly decreasing  $\delta_m$ . When  $\delta_m^2$  becomes comparable to variances of  $\mathcal{P}_m^h$  and  $\mathcal{P}_m^l$  the definition of  $\sigma_m^2$  becomes poorly defined, resulting in potentially large additions in consistent with the observed behavior in the background fields. Thus we truncate this procedure at  $m = 10$ , beyond which the shift is no longer statistically significant in any case.

This final component is then introduced to each realization of the stacked angular power spectra by adding an appropriate log-normal offset appropriate for the given choice of events. Because the variance of the background is determined using all 507 background fields, we renormalize the variance of the log-normal distribution to the number of source fields under consideration in the standard way, i.e.,  $\sigma_{m,\text{src}}^2 = \sigma_m^2 / N_{\text{src}}$ ; the  $\delta_m$  are unchanged. From this a set of angular power offsets are chosen and added to each realization of the angular power spectrum.

*Magnetic Field Strengths.*—In Fig. 13 we show the stacked angular power spectra for present day IGMF strengths of  $B_0 = 10^{-14}$  G,  $10^{-16}$  G, and  $10^{-17}$  G. These are directly comparable to Fig. 2, which shows  $B_0 = 10^{-15}$  G. These use the optimized source samples listed in [38], and thus differ for the null case and Poisson floor. As discussed in the main text, the quadrupole is considerably more than  $2\sigma$  discrepant for  $B_0 = 10^{-16}$  G,

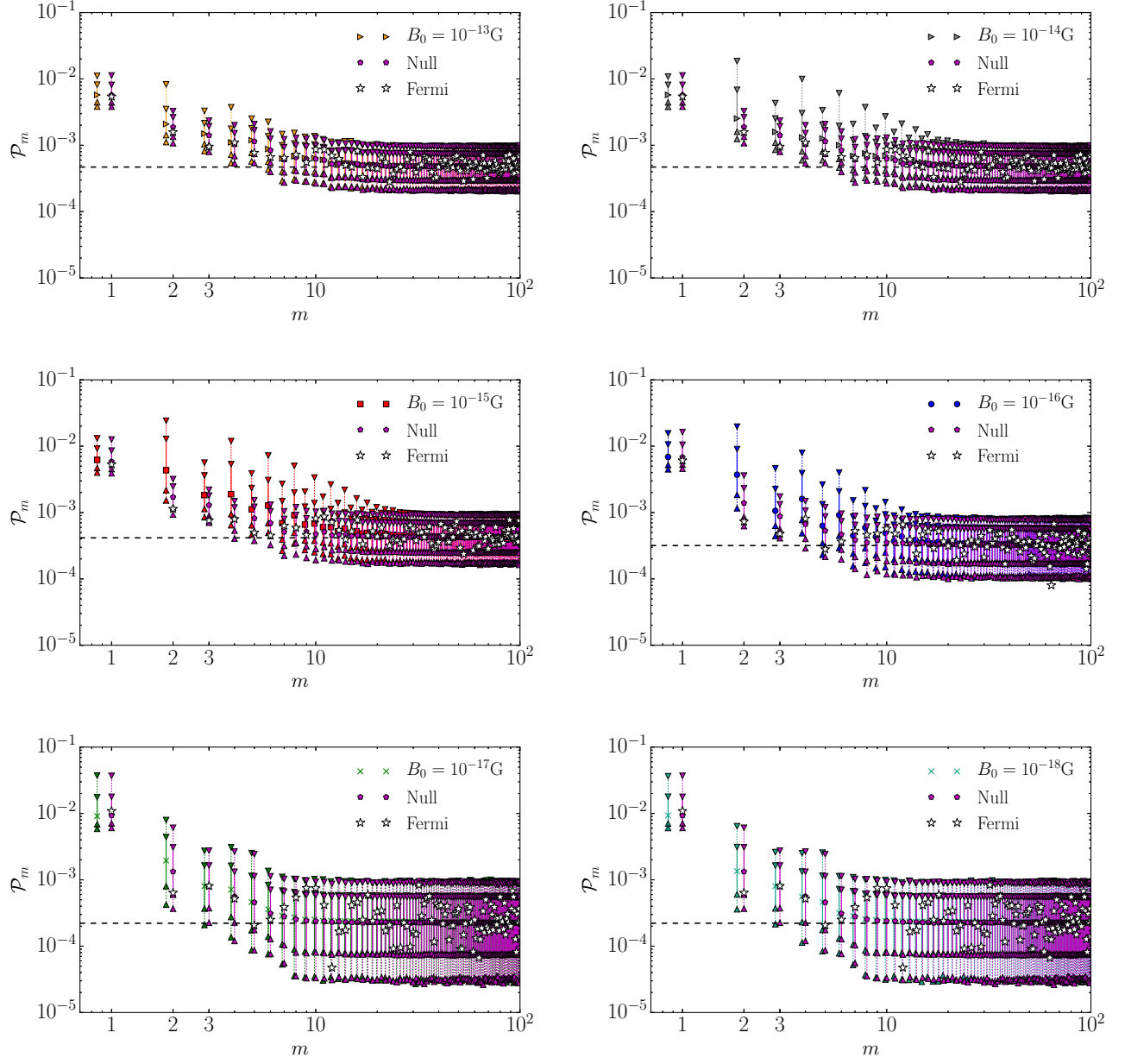


FIG. 13. Same as Fig. 2 in the main text for all of the IGMF strengths considered, i.e.,  $B_0 = 10^{-13}$  G,  $10^{-14}$  G,  $10^{-15}$  G,  $10^{-16}$  G,  $10^{-17}$  G, and  $10^{-18}$  G.

while the other field strengths are slightly less discrepant than  $2\sigma$ . In all cases the observed power is fully consistent with the null expectation.

*Font- vs. Back-Converted Events.*—In Fig. 14 we show the stacked angular power spectra for the optimized source list listed in [38] for a present day IGMF strength of  $B_0 = 10^{-15}$  G independently for Front- and Back-converted events. The observed quadrupolar power is discrepant with models that include inverse-Compton halos at  $2\sigma$  for both sets of events. Similarly, in both cases the

observed power is fully consistent with the null expectation. This conclusion holds for the other IGMF strengths considered.

*Power Correlations.*—Generally the powers at different multipoles are highly correlated when inverse-Compton halos are present [38]. As a result, we have not made an attempt to leverage the observed broad inconsistency with the halo model expectation at low  $m$ . Nevertheless, in Fig. 15 we show the joint probability distributions of the angular power in various low  $m$  multipoles

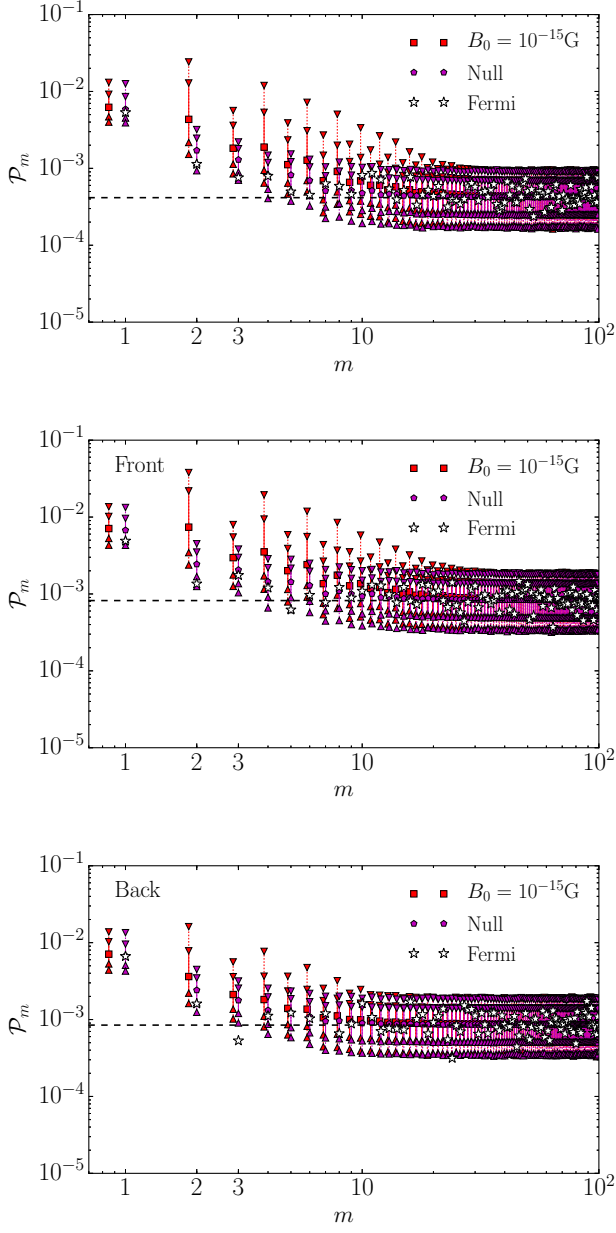


FIG. 14. Same as Fig. 2 in the main text for all photons (top), Front-converted photons only (middle) and Back-converted photons only (bottom). No significant difference is observed.

in comparison to the observed values. From the comparison when inverse-Compton halos are present (Fig. 15, left) it is clear that the observed powers lie well outside the joint distribution for all instances shown. That is, the observations are even more highly inconsistent than implied by the quadrupolar comparison we report in the main text. In contrast, when inverse-Compton halos are absent, i.e., our null case (Fig. 15, right), the discrepancy disappears.

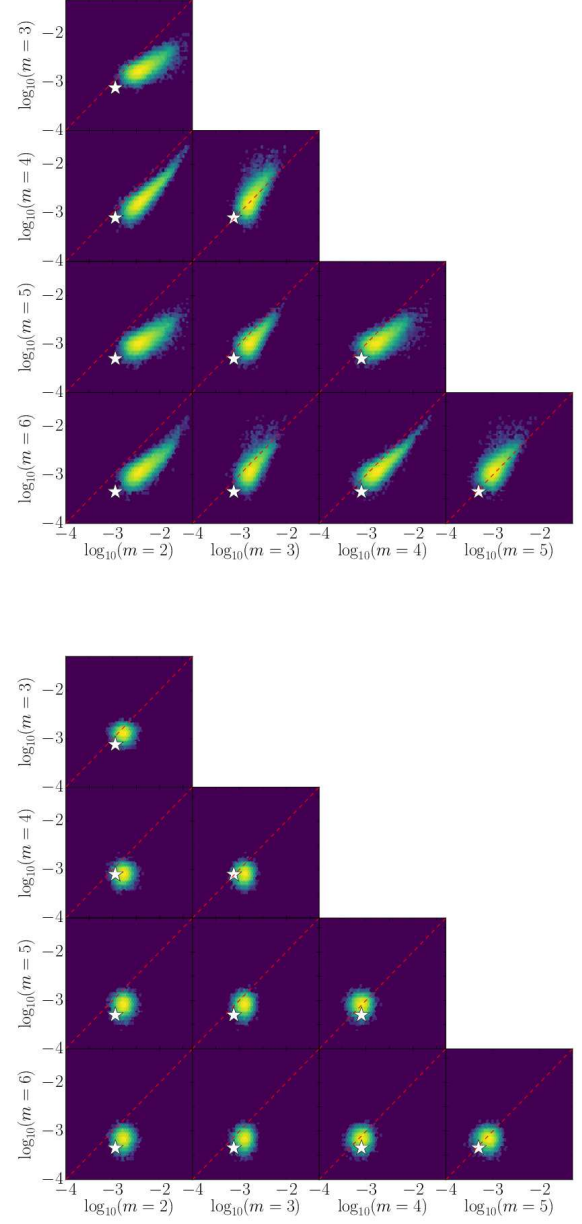


FIG. 15. Correlations in stacked angular power spectrum of the inverse-Compton halo (top) and Null (bottom) models (color map), in comparison to the observed values for a large-scale  $10^{-15}$  G IGMF (white star). In all panels the red dashed line shows the one-to-one relationship.